

Ag Nanoparticle-Sensitized WO₃ Hollow Nanosphere for Localized Surface Plasmon Enhanced Gas Sensors

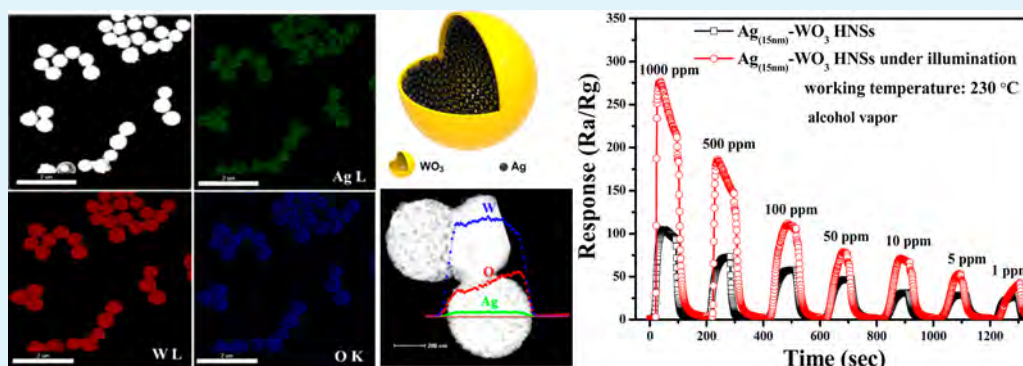
Yao Yao,^{†,‡} Fangxu Ji,[†] Mingli Yin,[†] Xianpei Ren,[†] Qiang Ma,[†] Junqing Yan,[†] and Shengzhong Frank Liu^{*,†,§}

[†]Key Laboratory of Applied Surface and Colloid Chemistry, National Ministry of Education; Shaanxi Engineering Lab for Advanced Energy Technology; School of Materials Science & Engineering, Shaanxi Normal University, Xi'an 710119, P. R. China

[‡]College of Chemistry and Chemical Engineering, Ningxia Normal University, Guyuan 756000, P. R. China

[§]Dalian Institute of Chemical Physics, Dalian National Laboratory for Clean Energy, Chinese Academy of Sciences, Dalian 116023, P. R. China

S Supporting Information



ABSTRACT: Ag nanoparticle (NP)-sensitized WO₃ hollow nanospheres (Ag-WO₃-HNSs) are fabricated via a simple sonochemical synthesis route. It is found that the Ag-WO₃-HNS shows remarkable performance in gas sensors. Field-emission scanning electron microscope (FE-SEM) and transmission electron microscope (TEM) images reveal that the Ag_x-WO₃ adopts the HNS structure in which WO₃ forms the outer shell framework and the Ag NPs are grown on the inner wall of the WO₃ hollow sphere. The size of the Ag NPs can be controlled by adjusting the addition amount of WCl₆ during the reaction. The sensor Ag_x-WO₃ exhibits extremely high sensitivity and selectivity toward alcohol vapor. In particular, the Ag_(15nm)-WO₃ sensor shows significantly lower operating temperature (230 °C), superior detection limits as low as 0.09 ppb, and faster response (7 s). Light illumination was found to boost the sensor performance effectively, especially at 405 and 900 nm, where the light wavelength resonates with the absorption of Ag NPs and the surface oxygen vacancies of WO₃, respectively. The improved sensor performance is attributed to the localized surface plasmon resonance (LSPR) effect.

KEYWORDS: Ag-WO₃, hollow nanosphere, sensor, plasmonic, alcohol

1. INTRODUCTION

Over the past decade, nanoscale semiconducting metal/metal oxide materials with special morphologies have emerged as promising resources for chemical sensors.¹ Tungsten oxide (WO₃), a popular *n*-type semiconductor for its sensitive dependence of electrical resistance on exposed atmosphere with a relatively wide band gap of 2.6 eV, is found to be an excellent chemical sensor material.^{2–14} In fact, it has exhibited an excellent response to a variety of poisonous, explosive, and volatile organic compounds (VOCs) including NO_x,^{2–4} H₂S,^{5,6} CO,⁷ H₂,⁸ ethanol,^{9–11} acetone,^{12–14} etc. Consider the assembly of 0D nanoparticle, WO₃ hollow nanospheres provide a high surface area for chemical reaction and a porous structure for effective gas diffusion and therefore exhibit better sensor performance than the bulk WO₃.^{12,15} Therefore, it is imperative

to develop more innovative nanostructures for even better and more useful WO₃-based sensors.

The combination of semiconductor and noble metal NPs are beneficial for enhancing sensing performance.¹⁶ In particular, when the metal oxides are integrated with metal nanoparticles with surface plasmonic generation, the combination may display unprecedented enhancement in light scattering, catalysis, biologic recognition, etc.¹⁷ Because of their high sensitivity to the surrounding atmosphere, localized surface plasmon resonance (LSPR) of metal nanoparticles can provide a unique pathway for chemical sensor research.^{11,18–21} Among

Received: April 19, 2016

Accepted: June 27, 2016

Published: June 27, 2016

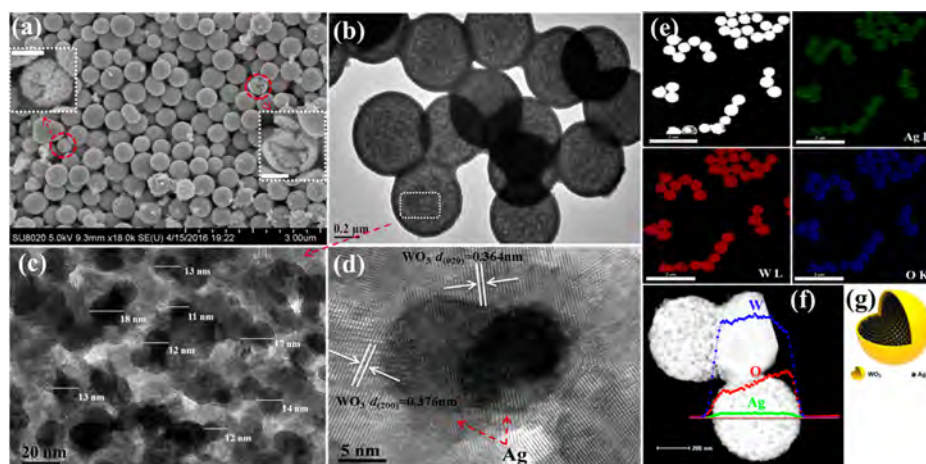


Figure 1. (a) Low- and high-magnification (inset) FE-SEM image of $\text{Ag}_{(15\text{nm})}\text{-WO}_3$ HNSs. Inset show a single cracked sphere. Scale bar: 200 nm. (b, c) TEM images of $\text{Ag}_{(15\text{nm})}\text{-WO}_3$ HNSs. (d) HR-TEM image of a representative area. STEM images and (e) EDX elemental mapping and (f) elemental line scans with respect to Ag, W, and O of $\text{Ag}_{(15\text{nm})}\text{-WO}_3$ HNSs. The diameters of Ag@C core-shell microspheres used in $\text{Ag}_{(15\text{nm})}\text{-WO}_3$ HNSs are $\sim 2 \mu\text{m}$. (g) Schematic diagram of $\text{Ag}_{(15\text{nm})}\text{-WO}_3$ HNSs.

well-known plasmonic metal elements, Ag is particularly attractive for its superior performance in visible spectrum with enhanced performance demonstrated for various devices.^{1,22–25}

Herein, to take all above advantages, we developed a sonochemical synthesis route for the direct growth of silver nanoparticles inside of the hollow WO_3 nanosphere using carbon for its weak reduction capability. The Ag nanoparticles (NPs) act as an effective inner shell to provide strong localized surface plasmon (LSP) excited across the visible spectrum. Meanwhile, WO_3 is often used as an effective LSPR host because its outer-d valence electrons could offer synergistic interactions with noble metal elements.^{26,27} Moreover, the LSP can be optimized by adjusting the diameter of the Ag nanoparticle.^{25,28,29} To systematically investigate the size effect of the Ag NPs, we synthesized a series of $\text{Ag}_x\text{-WO}_3$ HNSs and their sensing properties were also investigated. Compared with the sensor based on pure WO_3 HNSs, the $\text{Ag}_{(15\text{nm})}\text{-WO}_3$ HNS sensor shows much enhanced response toward alcohol vapor. It increases even more when it is illuminated. Moreover, the operation temperature is significantly reduced from 340 to 230 °C, and the detection limit for alcohol vapor was reduced to 0.09 parts-per-billion (ppb). Raman scattering of the $\text{Ag}_{(15\text{nm})}\text{-WO}_3$ shows significantly enhanced intensity, suggesting that the enhancement is due to nanoplasmonic mechanism.

2. EXPERIMENTAL SECTION

2.1. Materials. All chemicals including glucose ($\text{C}_6\text{H}_{12}\text{O}_6$), silver nitrate (AgNO_3), tungsten hexachloride (WCl_6), sodium hydroxide (NaOH), *N,N*-dimethylformamide (DMF), and ethanol are from Beijing Chemical Co., Ltd. Distilled water was used in the experiments unless otherwise specifically stated.

2.2. Fabrication of Ag@C core-shell nanoparticles. Ag@C NPs were prepared using an emulsion polymerization reaction of glucose under the hydrothermal condition during the synthesis process.^{30–32} In brief, glucose (8 g) was dispersed in deionized water (70 mL) to form a clear solution, and then 2.5 mL of 0.1 mol/L AgNO_3 aqueous solution was added drop by drop under vigorous stirring. After actively stirring for 30 min, the solution was added into a 100 mL Teflon-sealed autoclave, heated to 180 °C at 2 °C/min, and maintained at that temperature for 6 h. After cooling down to room temperature naturally, the solid sample was collected by centrifugation,

washed with deionized water and ethanol for several cycles, and then dried at 80 °C overnight.

2.3. Fabrication of $\text{Ag}_x\text{-WO}_3$ HNSs. The Ag-WO_3 HNSs were prepared by the controlled hydrolysis of WCl_6 in a coupling solvent with a little modification just as Li et al. reported.³³ WCl_6 was used as the metal precursor dissolved in DMF to form a 0.1 g/mL solution. Freshly prepared Ag@C NPs (0.2 g) were dispersed in 60 mL of DMF solution with the aid of ultrasonication, and then the appropriate amount of the WCl_6 solution was added under active ultrasonication. After ultrasonication for ~ 30 min, 1 mL of H_2O was added to ensure the hydrolyzation. The resulting suspension was aged for 24 h at room temperature after going on continuous ultrasonication for 1 h, and then filtered, washed with ethanol and deionized water, and dried at 80 °C in an oven for overnight. The resultant nanospheres were heated to 450 °C in air at 1 °C/min, with 30 min holding at 400 °C and kept at 450 °C for 60 min, and cooled down to room temperature naturally.

The size of the Ag NPs in the Ag-WO_3 HNSs can be controlled by adjusting the mass ratio of WCl_6 and templates (Ag@C), and/or the pH value during the reaction, and their preparation processes are listed in Supporting Information, Table S1, with the sample ID referenced by formula $\text{Ag}_{(\text{diameter})}\text{-WO}_3$ HNSs as $\text{Ag}_{(50\text{nm})}\text{-WO}_3$, $\text{Ag}_{(15\text{nm})}\text{-WO}_3$, and $\text{Ag}_{(5\text{nm})}\text{-WO}_3$. For the sake of comparison, pure WO_3 HNSs were also synthesized using the carbon nanospheres as the templates under the same preparation procedure without the addition of AgNO_3 .

2.4. Characterization. The phase compositions of the Ag-WO_3 HNSs samples were characterized by a DX-2700 X-ray diffractometer (XRD) with $\text{Cu K}\alpha$ radiation ($k = 0.15418 \text{ nm}$) in 2θ range of 20–80°. The transmission electron microscope (TEM) images and high-resolution TEM (HR-TEM) images were taken by a JEM-2100 JEOL TEM with the accelerating voltage of 200 kV. The element overlay was taken by a field-emission transmission electron microscope (FE-TEM, Tecnai G2 F20 FEI, with accelerating voltage of 200 kV) with an attachment of energy-dispersive analysis of X-ray (EDX). The morphologies of the samples were observed using a field-emission scanning electron microscope (FE-SEM, Hitach SU8020). Elemental analysis was performed on an AXIS ULTRA X-ray photoelectron spectroscopy (XPS) instrument (Kratos Analytical Ltd.) with a monochromatic X-ray source ($\text{Al K}\alpha$), using adventitious carbon ($\text{C } 1s = 284.6 \text{ eV}$) as the calibration reference. Gas-sensing tests were performed using a CGS-1TP gas sensitivity instrument (Beijing Elite Tech Co., Ltd., China).

2.5. Gas-sensing measurements. The sensor device was prepared as follows: the as-synthesized hollow nanosphere samples were ground with a few drops of deionized water before they were coated onto the ceramic substrate (6 mm \times 3 mm \times 0.5 mm) with Ag–Pd interdigital electrodes (0.15 mm). The changes of the

resistance of the device in dry air and testing gas atmosphere were measured by a CGS-1TP gas sensitivity instrument, defined as R_a and R_g , respectively. The sensor response (R_s) is defined as R_a/R_g in reducing gas atmosphere or R_g/R_a in oxidizing gas atmosphere. The response and recovery times are defined as the time taken by the sensor to achieve 90% of the entire resistance change for target gas adsorption and desorption, respectively.^{34,35} The device was examined in the temperature range of 25–350 °C at various concentrations of alcohol vapor (1–1000 ppm) in a temperature-controlled environment.³⁶

3. RESULTS AND DISCUSSION

3.1. Characterization of the Ag_x - WO_3 HNSs. The morphology and nanostructure of the Ag_x - WO_3 HNSs are examined by FE-SEM, TEM, and HR-TEM. Figure 1a,b shows the FE-SEM and TEM images of the $Ag_{(15nm)}$ - WO_3 HNSs with uniform size of hollow spheres ~500 nm in diameter, and it is composed of a large number of WO_3 nanocrystals. The walls of the spheres seem to be porous and structurally robust. Figure 1c reveals that the walls of the hollow spheres are decorated by numerous small Ag nanocrystals, ~15 nm in diameter. High-resolution transmission electron microscopy is used to characterize the detailed distribution of crystal planes, as shown in Figure 1d. The lattice fringes of a representative area have spacing of ca. 0.364 and 0.376 nm, well in line with the interplane spacing of WO_3 for the (020) and (200) crystal planes, respectively. We noticed that all lattice fringes are assigned to WO_3 , with none from Ag NPs, suggesting that innumerable Ag NPs are uniformly anchored on the internal wall of WO_3 HNSs. The EDX elemental mapping analysis is used to determine the chemical composition of the hollow sphere (Figure 1e). It confirms that the $Ag_{(15nm)}$ - WO_3 HNS sample consists of W, O, and Ag. The Ag is uniformly distributed in the entire nanosphere, forming a Ag - WO_3 hollow nanostructure. The line-scanning EDX signal (Figure 1f) shows that, at the outer surface of the sphere, the W and O signal rise simultaneously. The slight increase of the O signal traversing left to right across the particle is likely due to desorption of oxygen-containing species caused by the electron beam heating used for the analysis. In comparison, the Ag signal shows a delay by ~20 nm, indicating that the WO_3 shell thickness is ~20 nm, while the Ag NPs binds within the sphere. All three elemental signals show a plateau in the middle section, indicating that the Ag NPs are uniformly distributed, as illustrated in Figure 1g.

For comparison, the SEM and TEM images of other samples are provided in the Supporting Information. Figure S2a–c shows the sample $Ag_{(50nm)}$ - WO_3 HNSs constructed using ~50 nm Ag core prepared using 0.2 mol/L NaOH solution as the hydrolytic agent to maintain the $Ag@C$ template structure, as listed in Supporting Information Table S1. When the amount of WCl_6 was increased to 0.24 g, the hollow spheres appear irregular and Ag NPs are aggregated into smaller sizes (Figure S2d–f), indicating that low pH value may accelerate the dissolution and regrowth of Ag NPs, resulting in the formation of irregular particles. The corresponding sample is labeled as $Ag_{(5nm)}$ - WO_3 HNSs, and the Ag NPs are ~5 nm in diameter.

XRD is a powerful tool in providing crystalline structure information.³⁷ Figure 2a shows XRD patterns of the Ag_x - WO_3 HNSs and pure WO_3 for comparison. It shows that the WO_3 is monoclinic with space group: $P21/n(14)$ (JCPDS card no. 43-1035) while the Ag NPs are face-centered-cubic with space group: $Fm\bar{3}m(225)$ (JCPDS card no. 04-0783). There is no additional peak detected in the XRD analysis. As the WCl_6

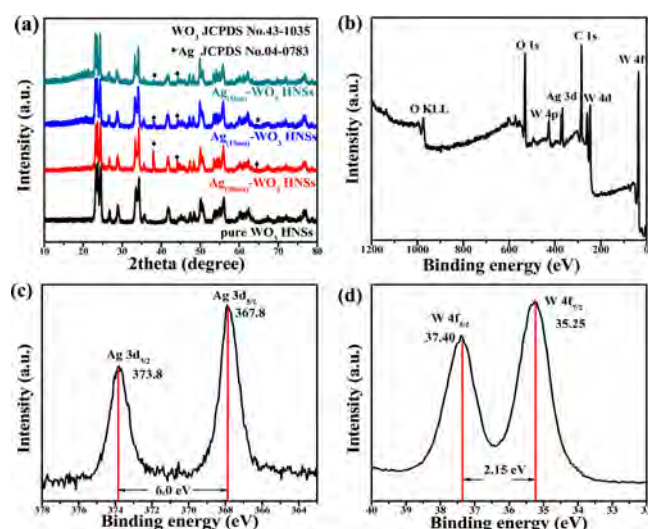


Figure 2. (a) XRD patterns of samples of pure WO_3 , $Ag_{(50nm)}$ - WO_3 HNSs, $Ag_{(15nm)}$ - WO_3 HNSs, and $Ag_{(5nm)}$ - WO_3 HNSs. Typical XPS spectra of $Ag_{(15nm)}$ - WO_3 HNSs samples (b) in a wide survey scan, (c) Ag 3d region, and (d) W 4f region.

concentration increases, the Ag peaks become weaker. The different peak intensities are compatible with the formation of Ag crystals of different dimensions, suggesting that the size of the Ag NPs is getting too small and the crystalline structure is becoming too frail to be detected by the XRD in the $Ag_{(5nm)}$ - WO_3 sample,³⁸ consistent with the TEM results. The chemical composition of the Ag_x - WO_3 HNSs was examined using X-ray photoelectron spectroscopy (XPS) as shown in Figure 2b–d. The survey-scan spectrum in Figure 2b demonstrates that the sample consists mainly of W, Ag, O, and C. The obvious C 1s peak is mainly from the $Ag@C$, and the carbon tape is used to fix the sample for the XPS measurement. Figure 2d shows two peaks at 35.2 and 37.4 eV, representing signatures of $W\ 4f_{7/2}$ and $W\ 4f_{5/2}$ of WO_3 respectively. Likewise, Figure 2c shows two peaks located at 367.8 and 373.8 eV assigned to $Ag\ 3d_{5/2}$ and $Ag\ 3d_{3/2}$ of metallic Ag, respectively.^{39,40} The XPS spectra reconfirm that the $Ag_{(15nm)}$ - WO_3 HNSs consist of WO_3 and metallic Ag, in good agreement with the XRD result.

Figure 3a shows the UV–vis–NIR spectra for all samples with the intrinsic absorption starting at 480 nm, corresponding to a band gap of WO_3 of 2.6 eV. The optical absorption beyond the band edge is due to the new discrete energy bands below the conduction band, and the absorption in the near-infrared region is attributed to the WO_3 with oxygen vacancies.⁴¹ The well-known characteristic plasmonic absorption peak of Ag NPs

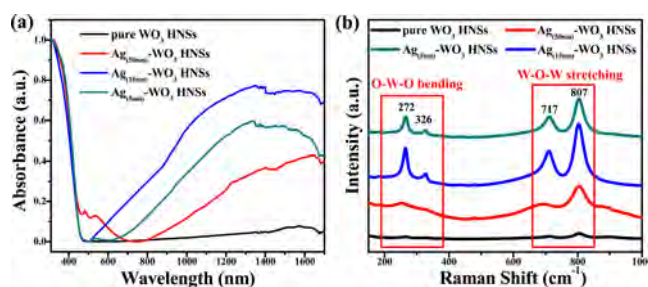


Figure 3. (a) UV–vis–NIR spectra and (b) Raman spectra of pure WO_3 , $Ag_{(50nm)}$ - WO_3 HNSs, $Ag_{(15nm)}$ - WO_3 HNSs, and $Ag_{(5nm)}$ - WO_3 HNSs.

is at ~ 405 nm,⁴² which is buried under the WO_3 band absorption. Compared with the pure WO_3 without oxygen vacancies (Figure S9), the LSPR absorption peak at ~ 1500 nm of $\text{Ag}_{(15\text{nm})}\text{-WO}_3$ increases significantly. However, when the Ag NPs was reduced to 5 nm, the absorption peak decreased. For $\text{Ag}_{(50\text{nm})}\text{-WO}_3$ HNSs, a red-shift of optical absorption and a decrease in the intensity of the plasmon are also observed, as explained by the incorporation of oxygen into the lattice, leading to a decrease in the carrier concentration.²⁶ This result suggests that the size and position of Ag NPs may play a key role in this process, as the SP adsorption shows a strong correlation with the Ag NP diameter.⁴³ The introduction of oxygen vacancies does not leave obvious XPS signatures (Figure 2d), as the W^{5+} peak may overlap with that of the W^{6+} .⁴¹ Figure 3b shows a comparison of surface-enhanced Raman scattering (SERS) spectra from the as-prepared samples, using a 532.2 nm excitation. Four major vibration bands at 272, 326, 717, and 807 cm^{-1} are attributed to the bending vibration of $\delta(\text{O}-\text{W}-\text{O})$ and stretching vibration of $\nu(\text{W}-\text{O}-\text{W})$, respectively.⁴⁴ Compared with the pure WO_3 , all $\text{Ag}_x\text{-WO}_3$ samples show the enhancement of Raman intensity. In particular, $\text{Ag}_{(15\text{nm})}\text{-WO}_3$ shows Raman intensity enhanced by as much as 13 times, significantly higher than that from $\text{Ag}_{(50\text{nm})}\text{-WO}_3$ and $\text{Ag}_{(5\text{nm})}\text{-WO}_3$, increased by only 4- and 6-fold, respectively, demonstrating that SERS enhancement may be strongly dependent upon size of the Ag NPs.^{25,45-47}

3.2. Gas-sensing results. The $\text{Ag}_x\text{-WO}_3$ HNSs are found to be particularly useful in gas-sensing application. The gas-sensing measurements were performed on an intelligent gas-sensing analysis system (Beijing Elite Tech Co., Ltd., China); Figure 4a provides an equivalent circuit model for the gas sensors studied. The optimum working temperature was determined using the sensor response to 500 ppm alcohol

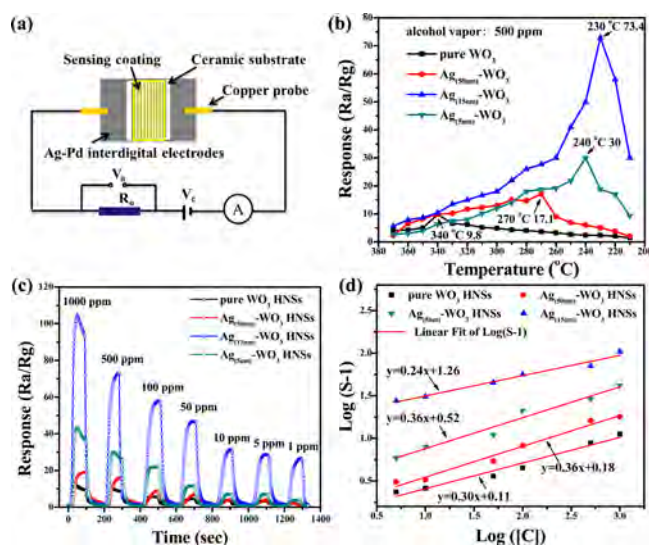


Figure 4. (a) Schematic device and measurement configurations. The sensing coating represents the $\text{Ag}_x\text{-WO}_3$ HNSs. (b) Responses of pure WO_3 , $\text{Ag}_{(50\text{nm})}\text{-WO}_3$ HNSs, $\text{Ag}_{(15\text{nm})}\text{-WO}_3$ HNSs, and $\text{Ag}_{(5\text{nm})}\text{-WO}_3$ HNSs to 500 ppm alcohol vapor at different working temperatures. (c) Dynamic responses curves of pure WO_3 , $\text{Ag}_{(50\text{nm})}\text{-WO}_3$ HNSs, $\text{Ag}_{(15\text{nm})}\text{-WO}_3$ HNSs, and $\text{Ag}_{(5\text{nm})}\text{-WO}_3$ HNSs to alcohol vapor of different concentrations at their respective optimum working temperature. (d) Linear relationship of $\log(S - 1) - \log[C]$ plot for the sensors of pure WO_3 , $\text{Ag}_{(50\text{nm})}\text{-WO}_3$ HNSs, $\text{Ag}_{(15\text{nm})}\text{-WO}_3$ HNSs, and $\text{Ag}_{(5\text{nm})}\text{-WO}_3$ HNSs.

vapor at different working temperatures, as shown in Figure 4b. It is clear that the sensor fabricated from $\text{Ag}_{(15\text{nm})}\text{-WO}_3$ HNSs shows the highest sensing response of 73.4, while the pure WO_3 , $\text{Ag}_{(50\text{nm})}\text{-WO}_3$, and $\text{Ag}_{(5\text{nm})}\text{-WO}_3$ show the responses of 9.8, 17.1, and 30, respectively. Moreover, the $\text{Ag}_{(15\text{nm})}\text{-WO}_3$ HNSs not only increase the responses by 7-fold compared to the pure WO_3 HNSs but also lower the optimum working temperature of sensor from 340 to 230 $^{\circ}\text{C}$. The large surface area and porosity of $\text{Ag}_{(15\text{nm})}\text{-WO}_3$ HNSs are beneficial for enhancing the performance of gas sensors. It is 16.15 m^2/g , about four times larger than that of the pure WO_3 HNSs (4.57 m^2/g); for details, see Supporting Information, Figure S3.

Figure 4c shows the dynamic response of the sensors upon repeated alcohol vapor exposure/removal cycles, corresponding to alcohol vapor concentrations from 1 to 1000 ppm. It is clear that sensors made of $\text{Ag}_x\text{-WO}_3$ HNSs show better performance than that of pure WO_3 , especially for the device using $\text{Ag}_{(15\text{nm})}\text{-WO}_3$. The resistance of $\text{Ag}_{(15\text{nm})}\text{-WO}_3$ changed significantly upon exposure to alcohol vapor and recovered immediately when vapor was removed. It shows an excellent recovery and high response to alcohol vapor, even at the gas concentration less than 10 ppm.

Figure 4d shows the correlation of the \log (sensor response) versus \log (alcohol concentration) at their respective optimum working temperature. On the basis of the empirical equation

$$S = 1 + a[C]^b$$

constants a and b are defined. It is obvious that $\log(S - 1)$ and $\log[C]$ give a linear correlation, with the slope of b value calculated from the plot, which is believed to represent oxygen ion species on the surface^{48,49} and/or morphology feature of the nanostructures.⁵⁰ The b is 0.5 for fully regular nanostructures, and it would deviate from 0.5 as the nanostructure become disordered or aggregated.^{50,51} In our work, both the b values of $\text{Ag}_x\text{-WO}_3$ HNSs (0.36, 0.24, and 0.36) and pure WO_3 HNSs (0.30) are significantly < 0.5 , indicating the hollow spherical shape of nanostructures. Furthermore, the sensor's theoretical detection limit of gas concentration $[C]_{\text{LOD}}$ can be obtained by extrapolating the linear fitted curve to $S = 3$. The sensor $\text{Ag}_{(15\text{nm})}\text{-WO}_3$ HNSs apparently exhibit excellent sensing performances. More specifically, the detection limit $[C]_{\text{LOD}}$ is as low as 0.09 ppb with the correlation coefficient $R = 0.97$, which is significantly better than that for the other three samples (4.37, 2.13, and 0.25 ppm; Supporting Information, Table S5).

The selectivity is another key parameter for practical gas sensors. Figure 5a shows the bar diagram of the sensor response to 50 ppm different target gases at 230 $^{\circ}\text{C}$. It is clear that the

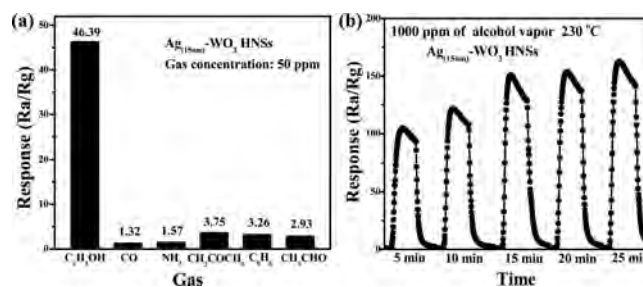
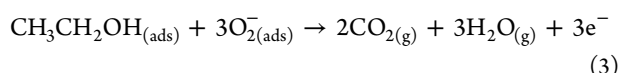
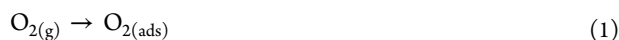


Figure 5. (a) Response of $\text{Ag}_{(15\text{nm})}\text{-WO}_3$ HNSs to 50 ppm different target gases at 230 $^{\circ}\text{C}$. (b) Transient response versus number of exposure test in 1000 ppm alcohol vapor at 230 $^{\circ}\text{C}$.

$\text{Ag}_{(15\text{nm})}\text{-WO}_3$ HNS sensor exhibits the highest sensitivity of 46.4 toward alcohol vapor, while it shows only minimal responses to other gases and vapors including CO , NH_3 , CH_3COCH_3 , C_6H_6 , and CH_3CHO under the same test concentration, demonstrating that the sensor shows remarkably good selectivity to alcohol. It is relatively common to see that this type of sensor shows good selectivity to alcohol vapor. It is believed that the underlying mechanism is that the ethanol species has an inclined conformation that permits easier access of $-\text{OH}$ groups to the Ag surface, thereby forming molecularly chemisorbed ethanol, which is then dissociated by the chemisorbed ionic oxygen.⁵² The corresponding chemical reactions between oxygen molecules adsorbed on the WO_3 surface and ethanol molecules are^{53,54}



The comparison of transient response and number of the exposure test was investigated in order to examine the stability of the gas sensors. We examined the sensor response of $\text{Ag}_{(15\text{nm})}\text{-WO}_3$ HNSs toward 1000 ppm alcohol vapor at an optimum working temperature of 230 °C. The test cycles were repeated at 5 min intervals. Figure 5b shows the response measurement of the sensors $\text{Ag}_{(15\text{nm})}\text{-WO}_3$. It is apparent that the resistance response decreases significantly during the alcohol exposure while it recovers as soon as the vapor is removed. The sensor response is 105 initially, and it rises to 150 at the third exposure test and remains at that high value with excellent stability for the subsequent test cycles. We have conducted the stability test for 10 days, as shown in Supporting Information Figure S7. For the test, the sensor was tested at day 1 for 10 cycles; it was retested at days 2, 5, and 10, with 10 cycles for each day, with the sensor being exposed in ambient between the tests. The concentration of the ethanol vapor was 50 ppm, and the working temperature was at 230 °C. This shows that the sensor shows very consistent sensitivity without clear degradation, indicating that the $\text{Ag}_{(15\text{nm})}\text{-WO}_3$ sensor is stable.

Moreover, we also observed the light-enhanced gas-sensor performance under the irradiation of a 150 W xenon arc light source, as shown in Figure 6a. Compared with the sensor performance in the dark (Figure 4c), the response of the $\text{Ag}_{(15\text{nm})}\text{-WO}_3$ HNSs increased by ~200%. By contrast, the change in response of the other three samples was much lower, in agreement with what had been observed from the SERS and UV-vis-NIR results, showing that the particle size of Ag NPs plays the major role in light-enhanced sensor response. The graphical summary and data are included in the Supporting Information, Figure S6 and Table S2.

Figure 6b presents the response/recovery times of sensors fabricated using pure WO_3 HNSs and $\text{Ag}_{(15\text{nm})}\text{-WO}_3$ HNSs, with the enlarged part of the resistance change as shown in Supporting Information. Figure S5 shows the resistance change of the pure WO_3 HNSs and $\text{Ag}_{(15\text{nm})}\text{-WO}_3$ HNSs. Apparently, the resistance of $\text{Ag}_{(15\text{nm})}\text{-WO}_3$ HNSs decreases upon exposure to alcohol vapor and recovers completely to the initial value upon the system being purged in air. Compared to the pure WO_3 HNSs, the response and recovery times are shortened to 15 and 80 s, respectively. We also measured the resistance

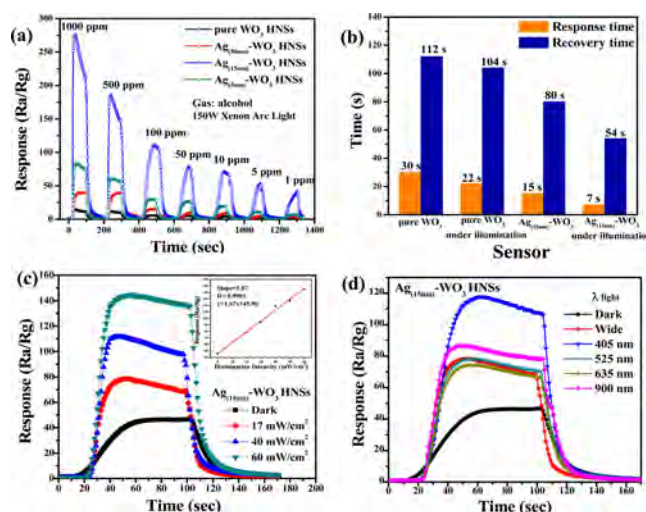


Figure 6. (a) Dynamic responses curves of pure WO_3 , $\text{Ag}_{(50\text{nm})}\text{-WO}_3$ HNSs, $\text{Ag}_{(15\text{nm})}\text{-WO}_3$ HNSs, and $\text{Ag}_{(5\text{nm})}\text{-WO}_3$ HNSs to alcohol vapor of different concentrations at the respective optimum working temperature under 150 W xenon arc light illumination. (b) Values of response and recovery times of pure WO_3 and $\text{Ag}_{(15\text{nm})}\text{-WO}_3$ HNSs to 500 ppm alcohol vapor at the respective optimum working temperature. (c) Sensor response of $\text{Ag}_{(15\text{nm})}\text{-WO}_3$ HNSs vs light illumination intensity using a xenon arc light source (150 W) attenuated by using neutral density filters. (Inset) The sensor response depends linearly on illumination intensity. (d) Sensor response of $\text{Ag}_{(15\text{nm})}\text{-WO}_3$ HNSs at different wavelengths of light-emitting diode (LED) irradiation.

change of $\text{Ag}_{(15\text{nm})}\text{-WO}_3$ HNSs toward 500 ppm alcohol vapor irradiated with xenon arc light, as shown in Figure S5d. Compared to the test in the dark circumstance, the light doubles the sensor response of $\text{Ag}_{(15\text{nm})}\text{-WO}_3$ HNSs and shortens the response and recovery times from 15 and 80 s to 7 and 54 s, respectively.

Figure 6c shows the dynamic responses of the $\text{Ag}_{(15\text{nm})}\text{-WO}_3$ HNS sensor toward 50 ppm alcohol vapor at 230 °C under a xenon arc light (150 W) illumination at different intensities, as attenuated by using neutral density filters. The sensor responses increased from 46 to 145 when the light illumination intensity changed from 0 to 60 mW/cm^2 (see Supporting Information Table S3 for more details). Furthermore, the sensor response has a linear dependence on the light intensity in the range of 0–60 mW/cm^2 , with a correlation coefficient $R = 0.9903$, indicating that the light irradiation intensity has a strong influence on the sensor response.

During the gas-sensing measurement, the $\text{Ag}_{(15\text{nm})}\text{-WO}_3$ is found to be the most sensitive sample. The size dependence on the catalytic activity and SPR effect of metal NPs is well-known.^{11,55} A good test to differentiate the “catalytic effect” and the “SPR effect” is to compare the sensor response under different wavelengths of light stimulation. The plasmonic effect would lead to (i) it being enhanced by the light irradiation; (ii) the enhancement factor being wavelength dependent; and (iii) the maximum enhancement at the wavelength coinciding with the LSPR absorption peak of the plasmonic NPs.²⁵ In our case, we measured sensor response as a function of light illumination wavelength using LEDs emitting at 405, 525, 635, and 900 nm. In the tests, the illumination intensity was attenuated to 17 mW/cm^2 for all wavelengths. Figure 6d shows that the $\text{Ag}_{(15\text{nm})}\text{-WO}_3$ HNS sensor response increased from 46 to 80 when it was illuminated (white light, 525 and 635 nm). Compared with

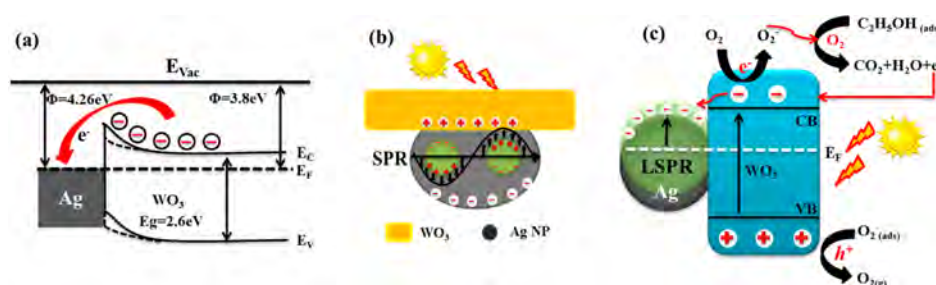


Figure 7. Schematic illustration (a) of the energy diagram and charge transfer process in the Ag-WO₃ HNSs; (b) for the surface plasmon resonance (SPR) effect of Ag nanoparticle; and (c) alcohol vapor sensing mechanism for Ag_x-WO₃ sensor in the presence of visible light.

using the white light, the sensor responses are increased by 150% and 110%, respectively, when irradiated at 405 and 900 nm, where the light wavelength resonates with the absorption of Ag NPs and the surface oxygen vacancies of WO₃. The illumination test for the pristine WO₃ was also conducted for comparison. As shown in Supporting Information Figure S8, it is found that the sensor response did not show significant wavelength-dependent performance. These results highlight the strong influence of light illumination on the Ag_(15nm)-WO₃ HNS nanosensor toward the alcohol vapor, indicating that LSP is the main reason for the improvement.

3.3. Enhancement mechanism. The remarkably enhanced gas-sensing performance by the Ag_x-WO₃ HNSs is attributed to the following aspects. First, the Ag_x-WO₃ HNSs provide higher surface-to-volume ratios, which are favorable for gas diffusion and adsorption, leading to enhanced sensor sensitivity.¹⁵ Second, as a *n*-type semiconducting metal oxide, oxygen vacancies in WO₃ lattice structure act as electron donors to provide electrons to their conduction band, and WO₃ has a small work function; therefore, electrons transfer from WO₃ to Ag when the Schottky junction is formed at the interface of Ag-WO₃,^{1,39} as illustrated in Figure 7a. The interfacial dipole layer leads to a negatively charged Ag surface and a positively charged WO₃ surface or the depletion zone.⁵⁶ At elevated temperature (230 °C) in air, the remnant electrons on the WO₃ surface are depleted due to the oxygen adsorption with negative charges,^{3,51} and the sensor resistance (*R*_a) is increased. When the reducing gas ethanol is injected, the dissociative adsorption happens on the surface of noble metal Ag first, and then the small molecule spills over to the WO₃ surface and reacts with chemisorbed ionic oxygen to produce CO₂ and H₂O,^{34,51,57,58} Then WO₃ obtains free electrons from the reaction and the current through the Schottky junction, and therefore the barrier height decreases to allow more electrons to pass through the junction; thus, the sensor resistance decreases (*R*_g), thereby yielding a high response.¹ When Ag NPs receive optical excitation energy, charge-density oscillation forms due to the surface plasmonic effect, leading to collective oscillation of electron density and consequently improved sensor response, particularly under illumination.^{11,26,47,59,60} (Figure 7b,c)

4. CONCLUSION

In conclusion, we have developed a novel nanostructure by assembling Ag nanocrystals on the inner shell surface of the WO₃ hollow nanospheres using a simple sonochemical synthesis route. It is found that the Ag_(15nm)-WO₃ HNS sensor shows higher response, better selectivity, shorter response/recovery times, lower detection limit, and lower optimum working temperature, which offers a potential platform for

practical application. We attribute the enhanced gas-sensor performance to (i) the high-opening surface area of the hollow nanostructure, (ii) the Ag-WO₃ Schottky junction, and (iii) the LSPR effect.

■ ASSOCIATED CONTENT

Supporting Information

The Supporting Information is available free of charge on the ACS Publications website at DOI: 10.1021/acsami.6b04692.

SEM images and TEM images of Ag_(50 nm)-WO₃ HNSs, Ag_(5 nm)-WO₃ HNSs, and Ag@C core-shell NPs; BET pattern and sensor performance including sensor response of as-prepared sensing device at different operating temperatures for 500 ppm alcohol vapor; resistance change of pure WO₃ and Ag_(15 nm)-WO₃ sensing device in dark and under illumination toward 500 ppm alcohol vapor at their optimum operating temperature; sensor response toward different concentrations of alcohol vapor at their optimum temperature in dark and under illumination; long-term stability of Ag_(15 nm)-WO₃; sensor response of pure WO₃ as a function of light illumination wavelength; experimental parameters and sensor performance data of various products (PDF)

■ AUTHOR INFORMATION

Corresponding Author

*Tel.: (+86) 180 9186 3826. E-mail: szliu@dicp.ac.cn.

Notes

The authors declare no competing financial interest.

■ ACKNOWLEDGMENTS

The authors acknowledge support from the National University Research Fund (GK261001009), the Changjiang Scholar and Innovative Research Team (IRT_14R33), the Overseas Talent Recruitment Project (B14041), and the Chinese National 1000-talent-plan program (1110010341)

■ REFERENCES

- (1) Basu, S.; Basu, P. K. Nanocrystalline Metal Oxides for Methane Sensors: Role of Noble Metals. *J. Sens.* **2009**, *2009*, 1–20.
- (2) Chen, D.; Yin, L.; Ge, L.; Fan, B.; Zhang, R.; Sun, J.; Shao, G. Low-Temperature and Highly Selective NO-Sensing Performance of WO₃ Nanoplates Decorated with Silver Nanoparticles. *Sens. Actuators, B* **2013**, *185*, 445–455.
- (3) Bai, S.; Zhang, K.; Luo, R.; Li, D.; Chen, A.; Liu, C. C. Low-Temperature Hydrothermal Synthesis of WO₃ Nanorods and Their Sensing Properties for NO₂. *J. Mater. Chem.* **2012**, *22* (25), 12643–12650.

- (4) López-Gándara, C.; Fernández-Sanjuán, J. M.; Ramos, F. M.; Cirera, A. Role of Nanostructured WO₃ in Ion-Conducting Sensors for the Detection of NO_x in Exhaust Gases from Lean Combustion Engines. *Solid State Ionics* **2011**, *184* (1), 83–87.
- (5) Li, Y.; Luo, W.; Qin, N.; Dong, J.; Wei, J.; Li, W.; Feng, S.; Chen, J.; Xu, J.; Elzatahry, A. A.; Es-Saheb, M. H.; Deng, Y.; Zhao, D. Highly Ordered Mesoporous Tungsten Oxides with A Large Pore Size and Crystalline Framework for H₂S Sensing. *Angew. Chem., Int. Ed.* **2014**, *53* (34), 9035–9040.
- (6) Datta, N.; Ramgir, N.; Kaur, M.; Roy, M.; Bhatt, R.; Kailasaganapathi, S.; Debnath, A. K.; Aswal, D. K.; Gupta, S. K. Vacuum Deposited WO₃ Thin Films Based Sub-ppm H₂S Sensor. *Mater. Chem. Phys.* **2012**, *134* (2–3), 851–857.
- (7) Ahsan, M.; Tesfamichael, T.; Ionescu, M.; Bell, J.; Motta, N. Low Temperature CO Sensitive Nanostructured WO₃ Thin Films Doped with Fe. *Sens. Actuators, B* **2012**, *162* (1), 14–21.
- (8) Gu, H.; Wang, Z.; Hu, Y. Hydrogen Gas Sensors Based on Semiconductor Oxide Nanostructures. *Sensors* **2012**, *12* (5), 5517–5550.
- (9) Zeng, W.; Li, Y.; Miao, B.; Pan, K. Hydrothermal Synthesis and Gas Sensing Properties of WO₃·H₂O with Different Morphologies. *Phys. E (Amsterdam, Neth.)* **2014**, *56*, 183–188.
- (10) Ma, J.; Zhang, J.; Wang, S.; Wang, T.; Lian, J.; Duan, X.; Zheng, W. Topochemical Preparation of WO₃ Nanoplates through Precursor H₂WO₄ and Their Gas-Sensing Performances. *J. Phys. Chem. C* **2011**, *115* (37), 18157–18163.
- (11) Xu, L.; Yin, M. L.; Liu, S. Ag_x@WO₃ Core-Shell Nanostructure for LSP Enhanced Chemical Sensors. *Sci. Rep.* **2014**, *4*, 6745.
- (12) Chen, D.; Hou, X.; Li, T.; Yin, L.; Fan, B.; Wang, H.; Li, X.; Xu, H.; Lu, H.; Zhang, R.; Sun, J. Effects of Morphologies on Acetone-Sensing Properties of Tungsten Trioxide Nanocrystals. *Sens. Actuators, B* **2011**, *153* (2), 373–381.
- (13) Choi, S. J.; Lee, L.; Jang, B. H.; Youn, D. Y.; Ryu, W. H.; Park, C. O.; Kim, I. D. Selective Diagnosis of Diabetes Using Pt-Functionalized WO₃ Hemitube Networks as A Sensing Layer of Acetone in Exhaled Breath. *Anal. Chem.* **2013**, *85* (3), 1792–1796.
- (14) Jia, Q.-q.; Ji, H.-m.; Wang, D.-h.; Bai, X.; Sun, X.-h.; Jin, Z.-g. Exposed Facets Induced Enhanced Acetone Selective Sensing Property of Nanostructured Tungsten Oxide. *J. Mater. Chem. A* **2014**, *2* (33), 13602–13611.
- (15) Lee, J.-H. Gas Sensors using Hierarchical and Hollow Oxide Nanostructures: Overview. *Sens. Actuators, B* **2009**, *140* (1), 319–336.
- (16) Majhi, S. M.; Rai, P.; Raj, S.; Chon, B. S.; Park, K. K.; Yu, Y. T. Effect of Au Nanorods on Potential Barrier Modulation in Morphologically Controlled Au@Cu₂O Core-Shell Nanoreactors for Gas Sensor Applications. *ACS Appl. Mater. Interfaces* **2014**, *6* (10), 7491–7497.
- (17) Das, S. K.; Marsili, E. Bioinspired Metal Nanoparticle: Synthesis, Properties and Application. In *Nanomaterials*; In Tech: 2011; [10.5772/25305](https://doi.org/10.5772/25305).
- (18) Bingham, J. M.; Anker, J. N.; Kreno, L. E.; Van Deyne, R. P. Gas Sensing with High-Resolution Localized Surface Plasmon Resonance Spectroscopy. *J. Am. Chem. Soc.* **2010**, *132*, 17358–17359.
- (19) Gogurla, N.; Sinha, A. K.; Santra, S.; Manna, S.; Ray, S. K. Multifunctional Au-ZnO Plasmonic Nanostructures for Enhanced UV Photodetector and Room Temperature NO Sensing Devices. *Sci. Rep.* **2014**, *4*, 6483.
- (20) Ghodselahe, T.; Zahrabi, H.; Saani, M. H.; Vesaghi, M. A. CO Gas Sensor Properties of Cu@CuO Core-Shell Nanoparticles Based on Localized Surface Plasmon Resonance. *J. Phys. Chem. C* **2011**, *115* (45), 22126–22130.
- (21) Cittadini, M.; Bersani, M.; Perrozzi, F.; Ottaviano, L.; Wlodarski, W.; Martucci, A. Graphene Oxide Coupled with Gold Nanoparticles for Localized Surface Plasmon Resonance Based Gas Sensor. *Carbon* **2014**, *69*, 452–459.
- (22) Wang, X.; Li, S.; Ma, Y.; Yu, H.; Yu, J. H₂WO₄·H₂O/Ag/AgCl Composite Nanoplates: A Plasmonic Z-Scheme Visible-Light Photocatalyst. *J. Phys. Chem. C* **2011**, *115* (30), 14648–14655.
- (23) Xiong, J.; Li, Z.; Chen, J.; Zhang, S.; Wang, L.; Dou, S. Facile Synthesis of Highly Efficient One-Dimensional Plasmonic Photocatalysts through Ag@Cu₂O Core-Shell Heteronanowires. *ACS Appl. Mater. Interfaces* **2014**, *6* (18), 15716–15725.
- (24) Zhu, M.; Chen, P.; Liu, M. Highly Efficient Visible-Light-Driven Plasmonic Photocatalysts Based on Graphene Oxide-Hybridized One-Dimensional Ag/AgCl Heteroarchitectures. *J. Mater. Chem.* **2012**, *22* (40), 21487–21494.
- (25) Rycenga, M.; Cobley, C. M.; Zeng, J.; Li, W.; Moran, C. H.; Zhang, Q.; Qin, D.; Xia, Y. Controlling the Synthesis and Assembly of Silver Nanostructures for Plasmonic Applications. *Chem. Rev.* **2011**, *111* (6), 3669–3712.
- (26) Manthiram, K.; Alivisatos, A. P. Tunable Localized Surface Plasmon Resonances in Tungsten Oxide Nanocrystals. *J. Am. Chem. Soc.* **2012**, *134* (9), 3995–3998.
- (27) Yin, Y.; Chen, M.; Zhou, S.; Wu, L. A General and Feasible Method for the Fabrication of Functional Nanoparticles in Mesoporous Silica Hollow Composite Spheres. *J. Mater. Chem.* **2012**, *22* (22), 11245–11251.
- (28) Lal, S.; Grady, N. K.; Kundu, J.; Levin, C. S.; Lassiter, J. B.; Halas, N. J. Tailoring Plasmonic Substrates for Surface Enhanced Spectroscopies. *Chem. Soc. Rev.* **2008**, *37* (5), 898–911.
- (29) Lee, K.-C.; Lin, S.-J.; Lin, C.-H.; Tsai, C.-S.; Lu, Y.-J. Size Effect of Ag Nanoparticles on Surface Plasmon Resonance. *Surf. Coat. Technol.* **2008**, *202* (22–23), 5339–5342.
- (30) Sun, X.; Li, Y. Ag@C Core/Shell Structured Nanoparticles: Controlled Synthesis, Characterization, and Assembly. *Langmuir* **2005**, *21*, 6019–6024.
- (31) Sun, S.; Wang, W.; Zhang, L.; Shang, M.; Wang, L. Ag@C Core/Shell Nanocomposite as A Highly Efficient Plasmonic Photocatalyst. *Catal. Commun.* **2009**, *11* (4), 290–293.
- (32) Li, D.; Wu, S.; Wang, Q.; Wu, Y.; Peng, W.; Pan, L. Ag@C Core-Shell Colloidal Nanoparticles Prepared by the Hydrothermal Route and the Low Temperature Heating-Stirring Method and Their Application in Surface Enhanced Raman Scattering. *J. Phys. Chem. C* **2012**, *116* (22), 12283–12294.
- (33) Li, X.-L.; Lou, T.-J.; Sun, X.-M.; Li, Y.-D. Highly Sensitive WO₃ Hollow-Sphere Gas Sensors. *Inorg. Chem.* **2004**, *43* (17), 5442–5449.
- (34) Yin, M.; Liu, M.; Liu, S. Development of An Alcohol Sensor Based on ZnO Nanorods Synthesized using A Scalable Solvothermal Method. *Sens. Actuators, B* **2013**, *185*, 735–742.
- (35) Park, S.; An, S.; Mun, Y.; Lee, C. UV-enhanced NO₂ Gas Sensing Properties of SnO₂-core/ZnO-shell Nanowires at Room Temperature. *ACS Appl. Mater. Interfaces* **2013**, *5* (10), 4285–4292.
- (36) Rai, P.; Khan, R.; Raj, S.; Majhi, S. M.; Park, K. K.; Yu, Y. T.; Lee, I. H.; Sekhar, P. K. Au@Cu₂O Core-shell Nanoparticles as Chemiresistors for Gas Sensor Applications: Effect of Potential Barrier Modulation on the Sensing Performance. *Nanoscale* **2014**, *6* (1), 581–588.
- (37) Liu, S.; Lu, Y.; KAPPES, M. M.; IBERS, J. A. The Structure of the C₆₀ Molecule: X-Ray Crystal Structure Determination of A Twin at 110 K. *Science* **1991**, *254*, 408–410.
- (38) Ma, B.; Guo, J.; Dai, W.-L.; Fan, K. Ag-AgCl/WO₃ Hollow Sphere with Flower-like Structure and Superior Visible Photocatalytic Activity. *Appl. Catal., B* **2012**, *123-124*, 193–199.
- (39) Chen, D.; Li, T.; Chen, Q.; Gao, J.; Fan, B.; Li, J.; Li, X.; Zhang, R.; Sun, J.; Gao, L. Hierarchically Plasmonic Photocatalysts of Ag/AgCl Nanocrystals Coupled with Single-Crystalline WO₃ Nanoplates. *Nanoscale* **2012**, *4* (17), 5431–5439.
- (40) Yin, X.; Que, W.; Fei, D.; Shen, F.; Guo, Q. Ag Nanoparticle/ZnO Nanorods Nanocomposites Derived by A Seed-mediated Method and Their Photocatalytic Properties. *J. Alloys Compd.* **2012**, *524*, 13–21.
- (41) Yan, J.; Wang, T.; Wu, G.; Dai, W.; Guan, N.; Li, L.; Gong, J. Tungsten Oxide Single Crystal Nanosheets for Enhanced Multi-channel Solar Light Harvesting. *Adv. Mater.* **2015**, *27* (9), 1580–1586.
- (42) Liu, Y.; Zi, W.; Liu, S.; Yan, B. Effective Light Trapping by Hybrid Nanostructure for Crystalline Silicon Solar Cells. *Sol. Energy Mater. Sol. Cells* **2015**, *140*, 180–186.

(43) Amendola, V.; Bakr, O. M.; Stellacci, F. A Study of the Surface Plasmon Resonance of Silver Nanoparticles by the Discrete Dipole Approximation Method: Effect of Shape, Size, Structure, and Assembly. *Plasmonics* **2010**, *5* (1), 85–97.

(44) Su, C.-Y.; Lin, H.-C.; Lin, C.-K. Fabrication and Optical Properties of Ti-doped $W_{18}O_{49}$ Nanorods using A Modified Plasma-Arc Gas-Condensation Technique. *J. Vac. Sci. Technol. B* **2009**, *27* (5), 2170–2174.

(45) Zhang, Q.; Li, W.; Moran, C.; Zeng, J.; Chen, J.; Wen, L.-P.; Xia, Y. Seed-Mediated Synthesis of Ag Nanocubes with Controllable Edge Lengths in the Range of 30–200 nm and Comparison of Their Optical Properties. *J. Am. Chem. Soc.* **2010**, *132*, 11372–11378.

(46) Maxwell, D. J.; Emory, S. R.; Nie, S. Nanostructured Thin-Film Materials with Surface-Enhanced Optical Properties. *Chem. Mater.* **2001**, *13*, 1082–1088.

(47) Anema, J. R.; Li, J. F.; Yang, Z. L.; Ren, B.; Tian, Z. Q. Shell-Isolated Nanoparticle-Enhanced Raman Spectroscopy: Expanding the Versatility of Surface-Enhanced Raman Scattering. *Annu. Rev. Anal. Chem.* **2011**, *4*, 129–150.

(48) Hongsih, N.; Wongrat, E.; Kerdcharoen, T.; Chooapun, S. Sensor Response Formula for Sensor Based on ZnO Nanostructures. *Sens. Actuators, B* **2010**, *144* (1), 67–72.

(49) Xu, L.; Yin, M.; Liu, S. Superior Sensor Performance from Ag@ WO_3 Core-Shell Nanostructure. *J. Alloys Compd.* **2015**, *623*, 127–131.

(50) Yao, M.; Li, Q.; Hou, G.; Lu, C.; Cheng, B.; Wu, K.; Xu, G.; Yuan, F.; Ding, F.; Chen, Y. Dopant-Controlled Morphology Evolution of WO_3 Polyhedra Synthesized by RF Thermal Plasma and Their Sensing Properties. *ACS Appl. Mater. Interfaces* **2015**, *7* (4), 2856–2866.

(51) Xue, X.; Chen, Z.; Ma, C.; Xing, L.; Chen, Y.; Wang, Y.; Wang, T. One-Step Synthesis and Gas-Sensing Characteristics of Uniformly Loaded Pt@ SnO_2 Nanorods. *J. Phys. Chem. C* **2010**, *114*, 3968–3972.

(52) Saito, N.; Inoue, Y. Effects of Thickness Extension Mode Resonance Oscillation of Acoustic Waves on Catalytic and Surface Properties I. Ethanol Decomposition on A Thin Ag Film Catalyst Deposited on Positively Polarized Z-Cut $LiNbO_3$. *J. Phys. Chem. B* **2002**, *106*, 5011–5016.

(53) Lyashkov, A. Y.; Tonkoshkur, A. S.; Makarov, V. O. Gas Sensing Properties of WO_3 -Based Ceramics to Ethanol Vapors. *Sens. Actuators, B* **2010**, *148* (1), 1–5.

(54) Ding, J.; Zhu, J.; Yao, P.; Li, J.; Bi, H.; Wang, X. Synthesis of ZnO-Ag Hybrids and Their Gas-Sensing Performance toward Ethanol. *Ind. Eng. Chem. Res.* **2015**, *54* (36), 8947–8953.

(55) Joy, N. A.; Nandasiri, M. I.; Rogers, P. H.; Jiang, W.; Varga, T.; Kuchibhatla, S. V.; Thevuthasan, S.; Carpenter, M. A. Selective Plasmonic Gas Sensing: H_2 , NO_2 , and CO Spectral Discrimination by A Single Au-CeO₂ Nanocomposite Film. *Anal. Chem.* **2012**, *84* (11), 5025–5034.

(56) Potje-Kamloth, k. Semiconductor Junction Gas Sensors. *Chem. Rev.* **2008**, *108* (2), 367–399.

(57) Shim, Y.-S.; Moon, H. G.; Kim, D. H.; Zhang, L.; Yoon, S.-J.; Yoon, Y. S.; Kang, C.-Y.; Jang, H. W. Au-Decorated WO_3 Cross-Linked Nanodomes for Ultrahigh Sensitive and Selective Sensing of NO_2 and C_2H_5OH . *RSC Adv.* **2013**, *3* (26), 10452–10459.

(58) Yin, M.; Liu, S. Preparation of ZnO Hollow Spheres with Different Surface Roughness and Their Enhanced Gas Sensing Property. *Sens. Actuators, B* **2014**, *197*, 58–65.

(59) Herminjard, S.; Sirigu, L.; Herzig, H. P.; Studemann, E.; Crottini, A.; Pellaux, J.-P.; Gresch, T.; Fischer, M.; Faist, J. Surface Plasmon Resonance Sensor Showing Enhanced Sensitivity for CO_2 Detection in the Mid-Infrared Range. *Opt. Express* **2009**, *17* (1), 293–303.

(60) Hu, D.; Diao, P.; Xu, D.; Wu, Q. Gold/ WO_3 Nanocomposite Photoanodes for Plasmonic Solar Water Splitting. *Nano Res.* **2016**, *9* (6), 1735–1751.